

Large-Area (Ag,Cu)(In,Ga)Se₂ Thin-Film Solar Cells with Increased Bandgap and Reduced Voltage Losses Realized with Bulk Defect Reduction and Front-Grading of the Absorber Bandgap

Alexandra M. Bothwell,* Siming Li, Rouin Farshchi, Michael F. Miller, Jake Wands, Craig L. Perkins, Angus Rockett, Aaron R. Arehart, and Darius Kuciauskas

The 1.24 eV bandgap, 18.8% power conversion efficiency Ag-alloyed chalcopyrite (Ag,Cu)(In,Ga)Se₂ (ACIGS) solar cells are characterized to relate voltage and efficiency improvements to electro-optical (EO) characteristics.


Shockley–Read–Hall recombination center defect density, identified and characterized through deep level transient spectroscopy and time-resolved photoluminescence (TRPL), is reduced through potassium and copper treatment optimization. Concomitantly, longer minority carrier lifetimes are achieved, which increases open-circuit voltage (V_{OC}). Near-conduction band defects associated in earlier studies with light-induced current instability are also mitigated. Analysis of charge-carrier dynamics after single- and two-photon excitation is used to separate recombination at the front interface and in the absorber bulk.

From TRPL decay simulations, the authors estimate ranges of key solar cell material characteristics: bulk carrier lifetime $\tau_{bulk} = 110\text{--}210$ ns, charge-carrier mobility $\mu = 110\text{--}160$ cm² V⁻¹ s⁻¹, and front interface recombination velocity $S_{front} = 700\text{--}1050$ cm s⁻¹. This lowest-reported S_{front} for ACIGS absorbers originates from the notched conduction band grading, which also makes the impact of the back interface recombination negligible. It is suggested in the results that solar cell performance enhancements can be made most readily with two distinct strategies: improving device architecture and reducing semiconductor defect densities. Using these approaches, power conversion efficiency in large-area solar cells is improved by 1.1% absolute.

1. Introduction

Record efficiency Cu(In,Ga)Se₂ (CIGS) solar cells typically have bandgaps between 1.08 and 1.13 eV.^[1–4] Power conversion efficiencies (PCEs) have reached 23.4% for small area cells (area = 1.04 cm²)^[1] and 19.2% for modules (area = 840 cm²)^[2] although the relatively narrow bandgaps inherently limit PCEs. For example, the single-junction Shockley–Queisser PCE limit for a 1.1 eV bandgap device is 32.2% while that of a 1.35 eV device is 33.1%.^[5] The Cu(In,Ga)Se₂ bandgap is set largely by the group III element ratio, [Ga]/([Ga]+[In]), or GGI,^[6,7] thus a wider E_g is realized with higher GGI (e.g., CuGaSe₂ devices have a 1.63 eV bandgap^[8]). However, when this strategy is employed for GGI > 0.4, voltage losses increase more than E_g such that PCE decreases.^[9–13] This has been attributed to a shorter minority carrier lifetime which, for example, changes from ≈ 400 ns for $E_g = 1.13$ eV to ≈ 0.2 ns for $E_g = 1.56$ eV for absorbers grown using a three-stage process.^[14] Although open-circuit voltage (V_{OC}) loss can be overcome in part by heavy

A. M. Bothwell, S. Li, C. L. Perkins, D. Kuciauskas
Materials, Chemical, and Computational Sciences
National Renewable Energy Laboratory
15013 Denver West Parkway, Golden, CO 80401, USA
E-mail: Alexandra.Bothwell@nrel.gov

 The ORCID identification number(s) for the author(s) of this article can be found under <https://doi.org/10.1002/solr.202200230>.

^[†]Present address: First Solar Inc., 1035 Walsh Ave., Santa Clara, CA 95050, USA

© 2022 The Authors. Solar RRL published by Wiley-VCH GmbH. This is an open access article under the terms of the Creative Commons Attribution-NonCommercial License, which permits use, distribution and reproduction in any medium, provided the original work is properly cited and is not used for commercial purposes.

DOI: 10.1002/solr.202200230

R. Farshchi^[†]
MiaSolé Hi-Tech Corp.
Santa Clara, CA 95051, USA

M. F. Miller, A. R. Arehart
Department of Electrical & Computer Engineering
The Ohio State University
Columbus, OH 43210, USA

J. Wands, A. Rockett
Colorado School of Mines
Golden, CO 80401, USA

alkali post-deposition treatments (PDT)^[3] and bandgap control through Ga grading,^[10,13,15] V_{OC} preservation in devices with bandgaps wider than the apparent industry standard of 1.08–1.13 eV is ultimately necessary for higher PCEs.

Another approach to widen the bandgap and improve V_{OC} is the partial substitution of Ag for Cu to form (Ag,Cu)(In,Ga)Se₂ (ACIGS) alloys. ACIGS absorbers have demonstrated bandgap widening with increasing Ag/(Ag+Cu) fraction,^[10] reduced lattice defects compared to their Cu(In,Ga)Se₂ counterparts (attributed to the lower melting temperature of the Ag-containing alloys),^[10] and maintenance of a single phase in films with Ag/(Ag+Cu) < 0.5.^[16] Reduced voltage loss and associated increased PCE has been documented for ACIGS devices^[17] and efficiencies have reached 20.56% in devices^[18] and 18.64% in modules.^[19] Earlier MiaSolé devices demonstrated successful Ag-alloying for 17.7% efficient ACIGS solar cells, but defect-associated metastabilities still persisted.^[20]

In this work, we study industrially manufactured ACIGS films and devices which incorporate Ag-alloying, optimized PDT and absorber grading to achieve a wide 1.24 eV bandgap, reduced voltage losses, and large-area (136.5 cm²) cell efficiencies of 18.8%. Through analysis of electro-optical (EO) properties, we attribute a 1.1% absolute PCE increase from 17.7%^[20] to longer minority carrier lifetime and reduced front interface recombination. Increased lifetime derives from decreased defect density in the absorber. Defect density in the bulk is directly measured with deep-level transient and deep-level optical spectroscopy (DLTS/DLOS). In contrast to material bulk improvement via defect reduction, reduced interface recombination derives from device design—an intentional grading profile near the front interface—and is evaluated from simulated one- and two-photon excitation (1PE and 2PE) time-resolved photoluminescence (TRPL) decays. The defect and EO characterization provide insight into properties of highly efficient ACIGS devices, origins of voltage improvements, and pathways for further advancements. This work demonstrates two distinct strategies for making more efficient solar cells—improving device architecture and reducing semiconductor defect densities. Such strategies apply to all solar cells and other electronic devices.

2. Results and Discussion

2.1. Solar Cell PCE, Absorber Bandgap, and Radiative Voltage

The ACIGS devices presented here were industrially fabricated at MiaSolé with an optimized potassium (K) PDT of the ≈10% Ag absorber and intentional bandgap grading. Details of the device fabrication and structure are given in Section 4. As demonstrated in **Figure 1a**, the large-area devices studied here achieved a PCE of 18.8%, V_{OC} = 777 mV, short-circuit current density J_{SC} = 31.5 mA cm⁻², and fill factor FF = 77.0%. Compared to our earlier report of 17.7% efficient Na- and K-treated ACIGS solar cells,^[20] improved photovoltaic performance of ACIGS devices in the current work was achieved with optimized K and Cu treatments on absorbers with a wider bandgap. A direct comparison between the current work and previous work by Ferguson et al.^[20] is provided in **Table 1**.

Although V_{OC} values are determined from current density–voltage (J – V) measurements under illumination, we do not expect that the light significantly reduced those values. TRPL measurements before and after 24-h light-soaking showed a decrease in tail lifetime from 56 to 48 ns. A simple estimation of the expected change in V_{OC} after light soaking is

Table 1. Parameter comparison between Ferguson et al.^[20] and current work.

Parameter	Ferguson et al. ^[20]	Current work
Absorber	Na, K-treated ACIGS	K-treated ACIGS
E_g	1.21 eV	1.24 eV
$V_{OC, max}$	742 mV	778 mV
$J_{SC, max}$	32.2 mA cm ⁻²	31.5 mA cm ⁻²
FF_{max}	74.0%	77.0%
η_{max}	17.7%	18.8%
Near-conduction band defect density	6.5×10^{15} cm ⁻³	7.2×10^{14} cm ⁻³
Mid-gap defect density	1.0×10^{14} cm ⁻³	4.3×10^{13} cm ⁻³
τ_{TRPL}	19 ns	56 ns

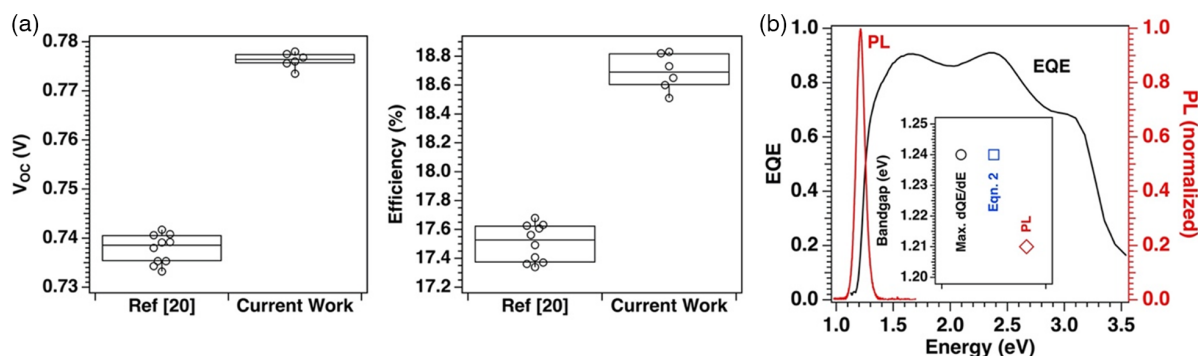


Figure 1. a) Current density–voltage (J – V) parameters highlight improvement in Ag-alloyed chalcopyrite (Ag,Cu)(In,Ga)Se₂ (ACIGS) device open-circuit voltage (V_{OC}) and efficiency with K and Cu optimization in this work. b) External quantum efficiency (EQE) and photoluminescence (PL) spectra of the optimized ACIGS device. Inset shows comparison of bandgap determination methods.

$\Delta V_{OC} = (kT/q) \cdot \ln(48 \text{ ns}/56 \text{ ns}) = -4.0 \text{ mV}$. Therefore, illumination for the short duration of J - V measurement should have negligible impact on measured V_{OC} .

The absorber bandgap was determined from external quantum efficiency (EQE) and PL emission spectra, both given in Figure 1b. From EQE, the bandgap was calculated by the method of Rau et al.^[21] where the distribution of Shockley–Queisser-type bandgap energies ($P(E_g)$) is given by

$$P(E_g) \frac{d}{dE} EQE(E). \quad (1)$$

The bandgap corresponds to the energy at the maximum, $P(E_g)_{max}$, or can be calculated as

$$E_g = \frac{\int_a^b E * P(E_g) dE}{\int_a^b P(E_g) dE} \quad (2)$$

where the integration limits, a and b , are equal to the energies at which $P(E_g)$ is half that of the maximum (equal to 1.204 and 1.278 eV for a and b , respectively, here). The bandgap calculated from Equation (1) and (2) was 1.24 eV, in agreement with the 1.24 eV energy at maximum $dEQE/dE$. The PL emission maximum at room temperature (1.21 eV) was only somewhat lower than the EQE-determined bandgaps, and the three bandgap determinations are given in the inset of Figure 1b. As reported by Carron et al.,^[22] PL methods underestimate absorber bandgap, particularly in CIGS, due to the presence of potential fluctuations. Therefore, we use the EQE-determined bandgap moving forward. The 1.24 eV bandgap is wider than earlier-reported MiaSolé ACIGS absorbers ($E_g = 1.21 \text{ eV}$, $V_{OC} = 742 \text{ mV}$, voltage deficit, $E_g/q - V_{OC} = 0.468 \text{ V}$),^[20] and the voltage deficit of 0.463 V is only 57 mV higher than for the record efficiency small area $E_g = 1.22 \text{ eV}$ device.^[17]

Given a 1.24 eV absorber bandgap, the Shockley–Queisser voltage is 988 mV for single-junction devices. The radiative V_{OC} ($V_{OC,rad}$) of the ACIGS device was 952 mV, calculated from EQE data as described by Krückermeier et al.,^[23] and given by

$$V_{OC,rad} = \frac{kT}{q} \ln \left(\frac{J_{SC}}{J_{0,rad}} + 1 \right) \quad (3)$$

k is Boltzmann's constant, T is temperature (K), q is the elementary charge, J_{SC} is determined from EQE, and $J_{0,rad}$ is radiative saturation current density. The radiative and measured V_{OC} differential of 175 mV in the 18.8% efficient device could be attributed to bulk recombination,^[24,25] sub-bandgap features,^[26] and interface recombination.^[27] A multipronged characterization approach was used to understand the V_{OC} loss mechanisms and origin of voltage improvements.

2.2. ACIGS Absorber Composition and Grading

Auger electron spectroscopy (AES) and secondary ion mass spectrometry (SIMS) depth profiles were measured to determine the Cu/(Cu+III) ratio, GGI, and bandgap grading throughout the absorber. In AES measurements, silver was not quantified due to an interference between the main silver peaks at 353 and 359 eV with an indium peak at 346 eV. Because composition

in our AES depth profiles is normalized to 100% at each sputtering cycle, absolute concentrations of Cu, Ga, In, and Se are slightly higher than they would be if silver had been included in the analysis. The AES profile, given in Figure 2a, showed a uniform Cu composition of approximately 24 at% and an average [Cu]/([Ga]+[In]) ratio of 0.9 in the bulk, and lower Cu content near the Mo back surface. The [Cu]/([Ga]+[In]) ratio indicates Cu-poor composition, which leads to p -type doping typically attributed to copper vacancies (V_{Cu}).^[28]

Point-to-point analysis of the depth-dependent AES atomic concentrations of Ga and In was performed to determine the GGI depth profile, shown in Figure 2b. These GGI data were used to calculate the bandgap according to $E_g = 1.68x + 1.03(1-x) - 0.12x(1-x)$ where $x = \text{GGI}$, under the assumption that ACIGS bandgap dependence follows that of CIGS.^[29] This assumption appears valid since the E_g minimum derived from chemical analysis in Figure 2b agrees with the bandgap derived from EQE in Section 2.1. The bandgap grading predominantly occurs in the conduction band as GGI primarily affects the conduction band energy. Therefore, grading can change minority carrier (electron) dynamics which, if done correctly, can result in reduced effective interface recombination.^[7] This aspect is analyzed in Sections 2.5 and 2.6.

AES was the primary compositional analysis technique because it is relatively simple to quantify, particularly near the film (front) surface where native oxides that are present can cause artifacts in SIMS. SIMS depth profiles, however, proved useful in quantifying silver content. As demonstrated in the SIMS data of Figure 2c, an Ag composition of $\approx 10\%$ was detected throughout the absorber, comparable to the composition of the target material. Figure 2d compares the GGI composition ratio determined by AES and SIMS. Good agreement between the two profiles at $x = 0.5$ – $1.5 \mu\text{m}$ corroborates that the absorber bandgap profile in Figure 2b is appropriate.

The V-shaped GGI profile, due to front region and back region absorber grading, is typical of high-efficiency Cu(In,Ga)Se₂ solar cells.^[30,31] The GGI profile is designed to minimize recombination: grading at the front is intended to reduce front interface recombination by reducing hole concentration at the junction and grading toward the back is intended to create a back surface field to direct minority carriers away from the high-recombination back surface.^[32] While the recombination rate at the absorber/Mo interface can be high, increasing E_g at the back by $>0.20 \text{ eV}$ reduces the impact of recombination.^[33] Our simulations, presented in Section 2.6, indicate that even when carriers are generated near the back contact by 2PE, they move away from the Mo interface within 1 ns after photogeneration, demonstrating the strong influence of bandgap grading on carrier movement in these devices.

2.3. Near-Conduction Band Defect Characterization

Near-conduction band traps in Cu(In,Ga)Se₂ solar cells have been hypothesized to play a large role in absorber electronic properties.^[34,35] Such defects can lead to band tails, increased recombination, and reduced charge-carrier mobility. While various defects and defect complexes can create shallow defects, experiments and first-principles calculations (Heyd-Scuseria-

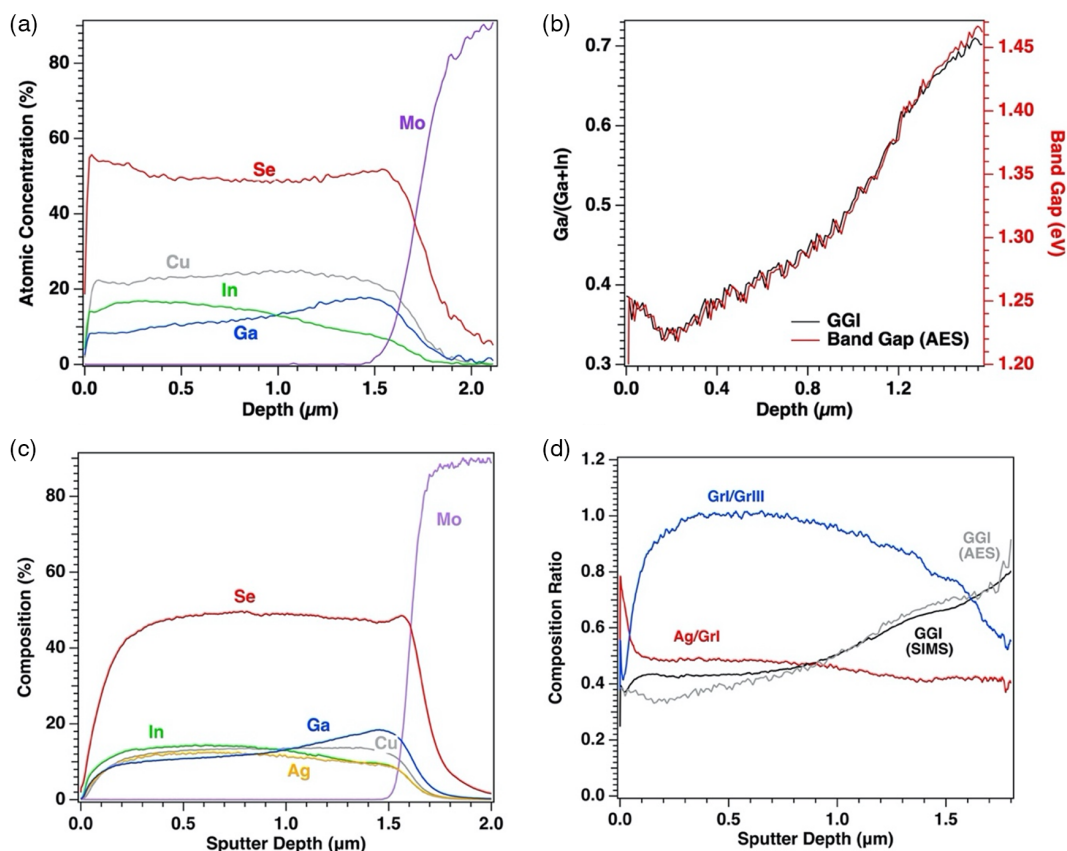


Figure 2. a) Auger electron spectroscopy (AES) depth profile for Ga, In, Cu, Se, and Mo and secondary ion mass spectrometry (SIMS) profile c) show increased Ga grading toward the back of the ACIGS absorber. b) The GGI depth profile and calculated bandgap from AES measurements highlight the Ga and bandgap grading throughout the absorber. d) AES and SIMS data show good agreement of GGI.

Ernzerhof (HSE06) hybrid functional in conjunction with the Vienna Ab initio simulation (VASP) density-functional theory code) attributed defects ≈ 150 mV below the conduction band minimum to the $V_{Se}-V_{Cu}$ divacancy,^[36] in agreement with the original Lany–Zunger model.^[35] These divacancies are also expected to contribute to optical metastabilities.^[36]

Shallow trap states were studied using PL emission and excitation spectroscopies and DLOS. Band-to-band and defect-mediated transitions can be characterized by PL emission measured at varied excitation fluences. The integrated emission intensity, I_{PL} , is described by a power law, $I_{PL} \propto P^k$, where P is excitation power and k is a constant. For $k > 1$, recombination is attributed to band-to-band transitions and for $k < 1$ recombination involves defect states.^[37] The inset of **Figure 3a** shows PL intensity versus excitation power (with a fluence range of 2.7×10^{14} – 6.7×10^{16} $\text{cm}^{-2} \text{s}^{-1}$) for temperatures of 300 and 5 K. Fits to the power law give $k = 1.64 \pm 0.06$ and 0.51 ± 0.01 for 300 and 5 K, respectively. This change in slope indicates PL emission at 300 K is primarily driven by band-to-band recombination while at 5 K PL emission is mostly due to defect states.

Temperature-dependent PL emission was used to probe defect versus band-to-band recombination. PL emission spectra in **Figure 3a** show a blueshift of +46 meV when temperature is increased from 5 to 300 K. An increase in full width at half

maximum (FWHM) from 63 meV (5 K) to 87 meV (300 K) was also observed. An energy increase with increasing temperature (while the bandgap is *decreasing* at higher temperature) is typical for chalcopyrites such as CIGS and is explained using bandgap and electrostatic fluctuation models.^[38] The log-scaled PL emissions at 5, 75, 100, 150, and 250 K in **Figure 3b** show that in addition to the main emission peak (labeled peak 1), a small amplitude shoulder at < 1 eV (labeled peak 2) was present at lower temperatures. This feature occurs at the same energy as the low energy peak in the PL excitation spectrum (discussed below) and is consistent with CIGS and ACIGS defect states reported in the literature.^[20,32,34,35]

To quantify the activation energy E_a for peaks 1 and 2, the amplitudes I were fit to the equation

$$I = \frac{I_0}{1 + A \exp\left(-\frac{E_a}{k_B T}\right)} \quad (4)$$

where k_B is the Boltzmann constant, T is temperature, and A and I_0 are constants. As shown in **Figure 3c**, the fit gives $E_a = 32 \pm 5$ meV for peak 1 and $E_a = 29 \pm 4$ meV for peak 2. While peak 2 energy is ≈ 250 meV below the bandgap, its activation energy is much smaller, suggesting the presence of multiple defect and sub-bandgap states.

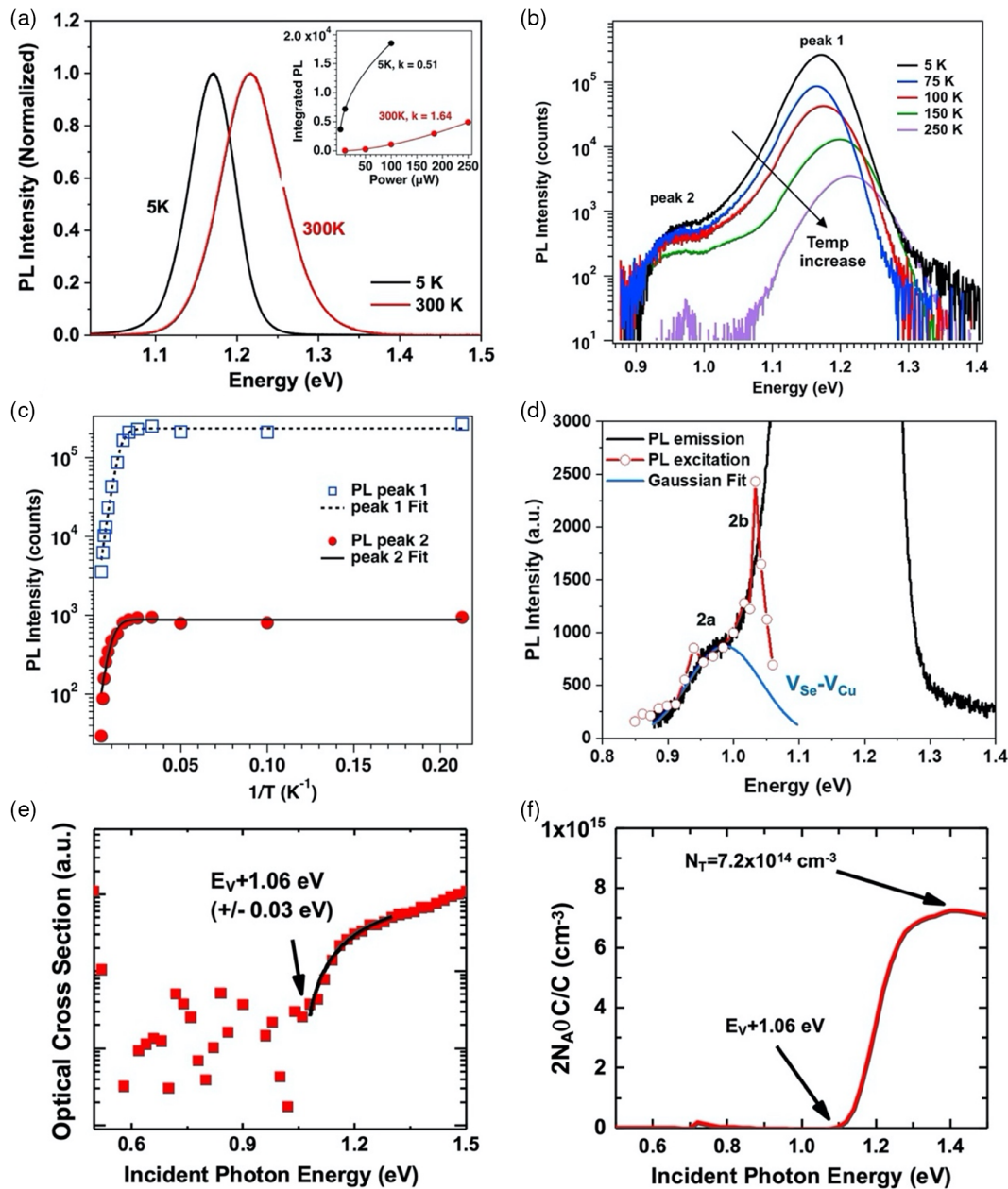


Figure 3. a) PL emission spectra at 5 K (black) and 300 K (red). The excitation-dependent PL intensity is given in the inset. Excitation ranged from 2.7×10^{14} – $6.7 \times 10^{16} \text{ cm}^{-2} \text{ s}^{-1}$ where 1-sun fluence = $3.2 \times 10^{17} \text{ cm}^{-2} \text{ s}^{-1}$. b) Temperature-dependent PL emission spectra, where peak 1 is near-bandgap emission and peak 2 is the low energy shoulder. c) Determination of activation energies of $32 \pm 5 \text{ meV}$ for peak 1 and $29 \pm 4 \text{ meV}$ for peak 2. d) Comparison of low-temperature PL emission and room-temperature excitation spectra. e) Deep-level optical spectroscopy (DLOS) fit with the Lucovsky model, which assumes no Franck–Condon energy (no lattice relaxation), indicates a trap at $E_V + (1.06 \pm 0.03 \text{ eV})$. f) The steady-state photocapacitance spectrum (SSPC) indicates the $E_V + 1.06 \text{ eV}$ trap has a concentration of $7.2 \times 10^{14} \text{ cm}^{-3}$ —determined by the step height of the SSPC spectrum.

Such states were explored further using PL excitation spectroscopy. Through variation in optical excitation energy, this technique probes defects within the absorber bandgap. The PL emission spectrum at 5 K and PL excitation spectrum at 300 K are overlaid in Figure 3d. The agreement between emission and excitation spectra is very good at $E \leq 1.02 \text{ eV}$. This region of the spectrum is approximated by a Gaussian

line shape with maximum at $1.00 \pm 0.01 \text{ eV}$ and $\text{FWHM} = 142 \pm 3 \text{ meV}$. We observed similar characteristics for CIGS fabricated at the National Renewable Energy Laboratory^[36] and earlier-generation ACIGS absorbers from MiaSolé.^[20] Positron annihilation spectroscopy (PAS) has been used to directly measure $V_{\text{Se}}-V_{\text{Cu}}$ defect densities and PAS indicated a similar chemical nature of the defect for CIGS and

ACIGS absorbers.^[20] Therefore, in this work, we attribute the 1.0 eV defect peak in Figure 3d to $V_{Se}-V_{Cu}$ divacancies.

The excitation spectrum in Figure 3d indicates a more complex defect structure than reported earlier.^[20,36] Here, a second narrow excitation peak at ≈ 1.04 eV is present. The difference between the 1.0 eV (peak 2a) and 1.04 eV (peak 2b) energies is similar to the activation energy E_a in Figure 3c, so temperature-dependent PL may indicate transitions between these states. Since first principles analysis was applied to simplified absorber models,^[34,36] the identity of multiple sub-peaks in these more complex absorbers is not known.

DLOS was used to measure densities of near-conduction band defect states, and the corresponding steady-state photocapacitance (SSPC) is given in Figure 3f. The trap energy was calculated by fitting the optical cross-section data (Figure 3e) using the Lucovsky photoionization model, which assumes no lattice relaxation (i.e., no Franck–Condon energy).^[39] The trap concentration was determined from the SSPC peak maximum. DLOS shows a defect at $E_V + (1.06 \pm 0.03)$ eV, and a trap density $N_T = 7.2 \times 10^{14} \text{ cm}^{-3}$. The Lucovsky model fits well, but it is possible a small Franck–Condon energy exists ($< \approx 0.05$ eV), which would lead to a separation of the PL emission and DLOS optical absorption for the trap. Nonetheless, the trap measured by PL and DLOS are of similar energy and are likely the same defect. This near-conduction band defect has been correlated with light-induced J_{SC} reduction, where devices with lower trap densities achieve superior J_{SC} stability.^[20,40] The $V_{Se}-V_{Cu}$ trap density of this device was notably smaller than Na- and K-treated ACIGS densities reported in literature,^[20] which suggests that the K and Cu optimization employed in these highly efficient ACIGS devices is a route for $V_{Se}-V_{Cu}$ defect density reduction and concomitant performance improvement.

2.4. Mid-Gap Trap Characterization

Mid-gap defect densities were determined with DLTS and their impact on recombination was evaluated using TRPL. The depletion region probed by DLTS, extracted from room-temperature capacitance–voltage (C–V) measured at 1 MHz, is given in the

carrier density profile in Figure 4a. The DLTS spectrum shown in Figure 4b reveals a single majority carrier trap with a trap concentration of $4.3 \times 10^{13} \text{ cm}^{-3}$. The calculation of the trap concentration includes a correction of 3.07 for the double boxcar t_2/t_1 ratio and correction for the difference between the depletion region volume and the actual volume where the traps are modulated—often referred to as lambda correction.^[41] This correction was 3.4X based on the doping and applied biases. Arrhenius analysis of the DLTS data, shown as an inset in Figure 4b, yielded an energy of $E_V + (0.58 \pm 0.05)$ eV. This trap has been observed in ACIGS absorbers previously and is likely due to a Cu_{In} or Cu_{Ga} antisite.^[42–44] The mid-gap trap concentration of $4.3 \times 10^{13} \text{ cm}^{-3}$ with K and Cu optimization was significantly reduced compared to previously reported $N_T = 1 \times 10^{14} \text{ cm}^{-3}$,^[20] which is possibly due to the Cu-poor growth of the ACIGS absorber. An associated increase in doping was measured in a carrier concentration increase to $\approx 3 \times 10^{15} \text{ cm}^{-3}$.

The TRPL lifetime of this device (56 ns, presented in Section 2.5) was approximately three times that of the previously reported ACIGS device.^[20] This is consistent with the measured decrease in mid-gap trap concentration and follows the expected relationship $\tau \propto 1/\sigma N_T V_{th}$ where σ is trap capture cross section, N_T is trap concentration, and V_{th} is thermal velocity. Despite the reduction in mid-gap trap concentration, it is still sufficiently high such that this defect will act as a Shockley–Read–Hall (SRH) recombination center and limit bulk lifetime, τ_{bulk} .^[45]

2.5. Carrier Dynamics from TRPL

To relate defect density determined with DLTS to carrier lifetimes, we analyze bulk and front interface recombination. To probe the front, 1PE TRPL was measured, where excitation photons have energy greater than the absorber bandgap and a large carrier concentration is generated near the front. To probe carrier dynamics in the absorber bulk, 2PE TRPL measurement utilizes photoexcitation at sub-bandgap energies such that through a two-photon absorption process carriers are generated nearly uniformly throughout the absorber.^[46] The 1PE and 2PE data are also simulated using the model described later and a

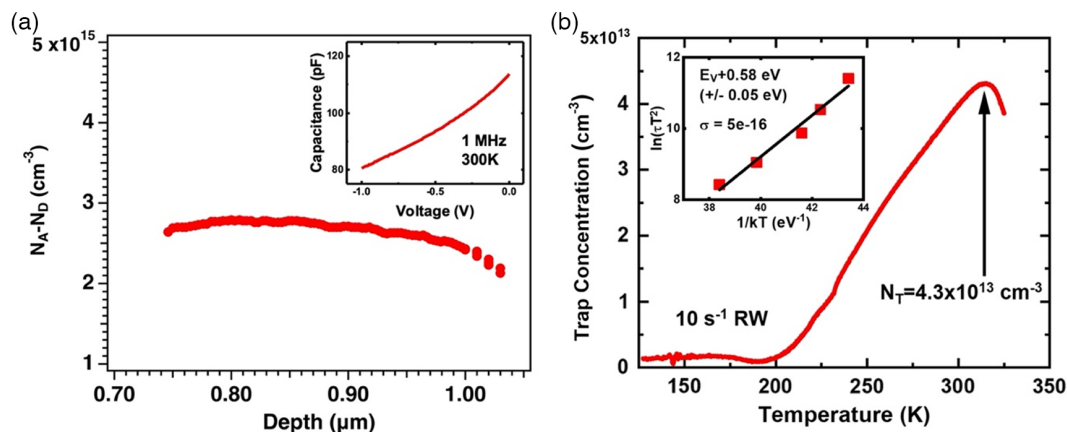


Figure 4. a) Carrier density profile indicates $\approx 3 \times 10^{15} \text{ cm}^{-3}$ carrier density with K and Cu optimization and inset show the raw capacitance–voltage (C–V) data. b) The 10 s^{-1} rate window from deep-level transient spectroscopy (DLTS) shows a deep defect with a concentration of $4.3 \times 10^{13} \text{ cm}^{-3}$ in the optimized ACIGS device. The Arrhenius inset shows linear fitting analysis for determination of $E_V + 0.58$ eV trap energy.

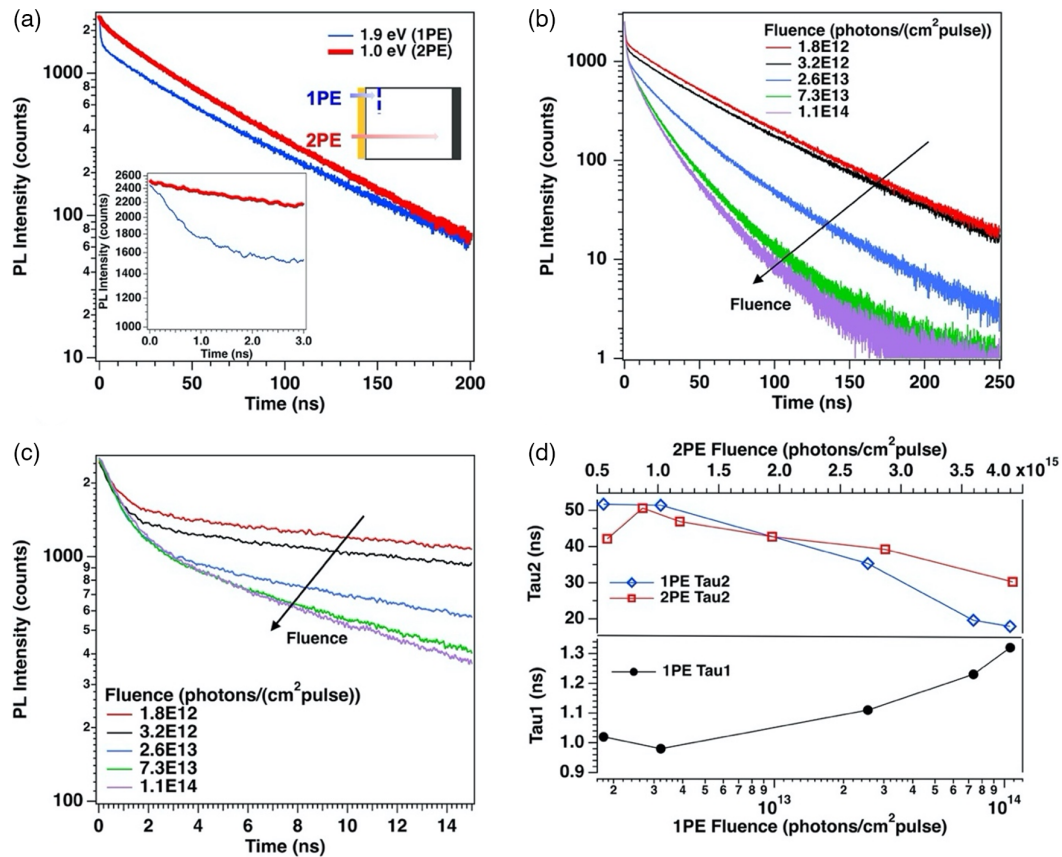


Figure 5. a) One-photon excitation (1PE) (excitation at 1.9 eV, fluence 3.2×10^{12} photons cm^{-2} pulse $^{-1}$) and 2PE (excitation at 1.0 eV, fluence 8.7×10^{14} photons cm^{-2} pulse $^{-1}$) time-resolved PL (TRPL) decays. Inset shows the same data on a shorter time scale. b,c) Fluence-dependent 1PE TRPL data on b) long and c) short time scales. d) 1PE and 2PE lifetimes versus excitation fluence.

common set of EO parameters. Using this approach, we establish ranges for bulk lifetimes, mobilities, and front interface recombination velocities consistent with the experimental data.

TRPL measurements were applied to absorbers with a CdS buffer layer. In this way, data directly show effects of absorber grading in high-efficiency ACIGS solar cells on carrier dynamics.^[47,48] The 1PE and 2PE TRPL decays are compared in Figure 5a, and the inset shows the initial decays of the same data (0–3 ns time scale). With 1PE, assuming an absorption coefficient $\alpha_{640\text{nm}} = 5 \times 10^4 \text{ cm}^{-1}$, more than 60% of carrier generation occurs within 0.2 μm of the front interface.^[49] As shown in Figure 5c, initial 1PE TRPL decay accounts for $\approx 50\%$ of the total and is independent of the photon fluence. Initial decay is attributed to minority carrier drift from the $E_g = 1.26$ eV front interface to the conduction band minimum ($E_g = 1.24$ eV). The E_g minimum is ≈ 0.2 μm from the CdS/ACIGS metallurgical interface (Figure 2b). Because the photo-generation profile is different with 2PE, the initial decay component is not present in the 2PE TRPL data, as shown in the inset of Figure 5a. Simulated low injection decay data (described later) provides quantitative deconvolution of interface recombination, drift, and bulk recombination.

Through fluence-dependent TRPL measurements, given in Figure 5b,c, we compare relative contributions of

defect-mediated SRH and radiative recombination. At the lowest 1PE excitation fluence, 1.8×10^{12} photons cm^{-2} pulse $^{-1}$, with 1.5 μm absorber thickness, the photogenerated carrier density is $1.2 \times 10^{16} \text{ cm}^{-3}$. When the fluence is increased by a factor of two, the shape of the TRPL decay is essentially unchanged (black and red in Figure 5b). This indicates that TRPL data are measured at low injection where SRH recombination dominates. Similar injection-independent dynamics in the low fluence range are observed with 2PE data (tail lifetimes, $\tau_{2,\text{TRPL}}$ are given in Figure 5d). The $\tau_{2,\text{TRPL}}$ decay times for 1PE and 2PE were 56 ± 1 and 55 ± 2 ns, respectively, determined by single-exponential fits to the low-fluence decay tails. Since these SRH recombination lifetimes include interface and bulk recombination, this indicates that bulk lifetime was greater than 56 ns in this structure.

With further increase in fluence, 1PE and 2PE TRPL lifetimes become shorter. This is a signature of bimolecular radiative recombination, which becomes increasingly important when the excitation fluence is increased.

Longer minority carrier (electron) lifetime leads to increased electron density and a change in the electron quasi-Fermi level. The resulting increase in voltage can be simply estimated. Compared to a previously reported ACIGS absorber TRPL tail lifetime of 19 ns,^[20] the 56 ns $\tau_{2,\text{TRPL}}$ lifetime measured in this

work should increase V_{OC} by $\Delta V_{OC} = (kT/q) \cdot \ln(56 \text{ ns}/19 \text{ ns}) = 28 \text{ mV}$. This accounts for 80% of the 35 mV measured V_{OC} increase and indicates that longer carrier lifetime is the dominant mechanism for V_{OC} improvement.

One limitation of analysis of TRPL decays measured on ACIGS/CdS structures is that it does not account for possible effects of window layer fabrication, which may alter front surface qualities such as defect states. Although the impact of window layer preparation on TRPL could not be explicitly evaluated in this work, the conclusions drawn in the preceding sections still hold. First, the decrease in defect density compared to Ferguson et al.^[20] of both the near-conduction band and deep defects was measured on completed solar cells and thus considers window layer preparation. Second, agreement of near-conduction band defect energy between DLOS (devices) and low-temperature PL (CdS/ACIGS) indicates that the near-bandgap defect energy remained unchanged after window preparation. Finally, the TRPL bulk lifetime and predicted V_{OC} increase was compared to unfinished ACIGS absorbers^[20] such that absorber improvements between the two structures are quantifiable.

2.6. Interface Recombination Velocity, Bulk Lifetime, and Charge-Carrier Mobility from 1PE and 2PE TRPL Simulations

TRPL simulations employed a MATLAB script developed by Weiss et al.,^[33] which calculates 1D PL transients by solving the drift-diffusion and continuity equations for electrons, n , and holes, p

$$\frac{dn}{dt} = D_n \frac{d^2n}{dx^2} + \mu_n \frac{dnE_n}{dx} - R \quad (5)$$

$$\frac{dp}{dt} = D_p \frac{d^2p}{dx^2} - R \quad (6)$$

D_n is the diffusion coefficient, μ_n is mobility, R is recombination rate, E_n is space charge field strength, t is time, and x is coordinate. Diffusion coefficient and mobility are related by $D = (\mu kT/q)$. The recombination rate includes radiative and SRH recombination. Interface recombination velocities S_{front} and S_{back} were incorporated through boundary conditions as described by Weiss et al. and Kanevce et al.^[33,50] Grading in the absorber was assumed to occur only in the conduction band, and the conduction band grading was created by linear interpolation of the AES GGI data between three points at the front, notch, and rear of the absorber (GGI = 0.386, 0.339, and 0.704, respectively).

PL transients were simulated by calculating the integral over the np product throughout the absorber as a function of time, given input parameters listed in **Table 2**. Parameters τ_{bulk} , μ , S_{front} , and S_{back} were varied in simulations. The absorption profile was implemented using the Beer–Lambert law

$$g(x, t) = exc \cdot pulse(t) \cdot A \cdot \exp(-\alpha x) \quad (7)$$

where exc is excitation photon fluence (7.8×10^{11} photons cm^{-2} pulse $^{-1}$), $pulse(t)$ is a Gaussian laser pulse (FWHM = 0.3 ps), x is depth into the absorber, and the A factor normalizes the exponential term. The 1PE and 2PE simulations were

Table 2. TRPL simulation parameters.

Parameter	Notation	Value
Radiative recomb. coefficient	B	$1.67 \times 10^{-10} \text{ cm}^3 \text{ s}^{-1}$
1.9 eV absorption coefficient	α	$5 \times 10^4 \text{ cm}^{-1}$
1.0 eV absorption coefficient	α	$1 \times 10^{-2} \text{ cm}^{-1}$
Absorber thickness	d	1.5 μm
Absorber doping	p_0	$3 \times 10^{15} \text{ cm}^{-3}$
Effective density of states	N_C, N_V	$2 \times 10^{18} \text{ cm}^{-3}$
Shallow trap density	N_t	$8 \times 10^{14} \text{ cm}^{-3}$
Temperature	T	300 K

differentiated by absorption coefficient: $\alpha = 5 \times 10^4 \text{ cm}^{-1}$ for 1PE (640 nm) and $\alpha = 1 \times 10^{-2} \text{ cm}^{-1}$ for 2PE (1200 nm).^[49]

Simulated 1PE and 2PE TRPL transients were compared to experimental data to determine ranges of τ_{bulk} , μ , and S_{front} values. We considered two cases of S_{back} : $1 \times 10^5 \text{ cm s}^{-1}$ and $1 \times 10^2 \text{ cm s}^{-1}$. By analyzing such two limiting cases, the back contact recombination is assessed without increasing the number of adjustable parameters.

Figure 6a summarizes simulation results for $S_{\text{back}} = 1 \times 10^5 \text{ cm s}^{-1}$. The range of EO parameters was unchanged for $S_{\text{back}} = 1 \times 10^2 \text{ cm s}^{-1}$, which indicates that the impact of back surface recombination is negligible due to the bandgap grading in this structure.

As shown in **Figure 6a**, bulk lifetime is between 110 and 210 ns ($\approx 1.9x$ variation), mobility between 110 and 160 cm^2 (Vs) $^{-1}$ ($\approx 1.5x$ variation), and S_{front} between 700 and 1050 cm s^{-1} ($\approx 1.5x$ variation). **Figure 6a** suggests that bulk lifetime and mobility are uncoupled: regardless of mobility, a range of bulk lifetimes is appropriate and vice versa. Simulations showed the mobility range was dictated primarily by fit to the initial τ_1 decay which is due to the dependence of τ_1 on charge separation and the electric field created by the bandgap grading. Constraint of the bulk lifetime was dictated by simulated and measured agreement for 2PE and tail 1PE data. Unlike the unbounded value from measurement alone, in this case, an upper limit of 210 ns was established. Bulk recombination lifetimes exceed measured lifetimes (**Figure 5**) because interface recombination also affects the decay tail.

We find that S_{front} influences both initial and tail decay components. The S_{front} range between 700 and 1050 cm s^{-1} is dictated not only by the defect density at the interface, but also by minority carrier drift from the interface. Drift occurs due to absorber grading, and it effectively reduces the impact of interface recombination. Thus, solar cell device design (bandgap grading at the front and back of the absorber) effectively mitigates interface recombination.

Figure 6b demonstrates simulated and measured 1PE and 2PE decays for a representative set of EO parameters. The initial τ_1 decay component for 1PE and the tail lifetime component for 1PE and 2PE data are well replicated.

Figure 6c,d shows simulated electron concentrations, $n(x)$, at increasing times post-laser pulse for 1PE and 2PE, respectively, where data correspond to TRPL decays in **Figure 6b**. For 1PE, electrons accumulate near the front-side bandgap notch

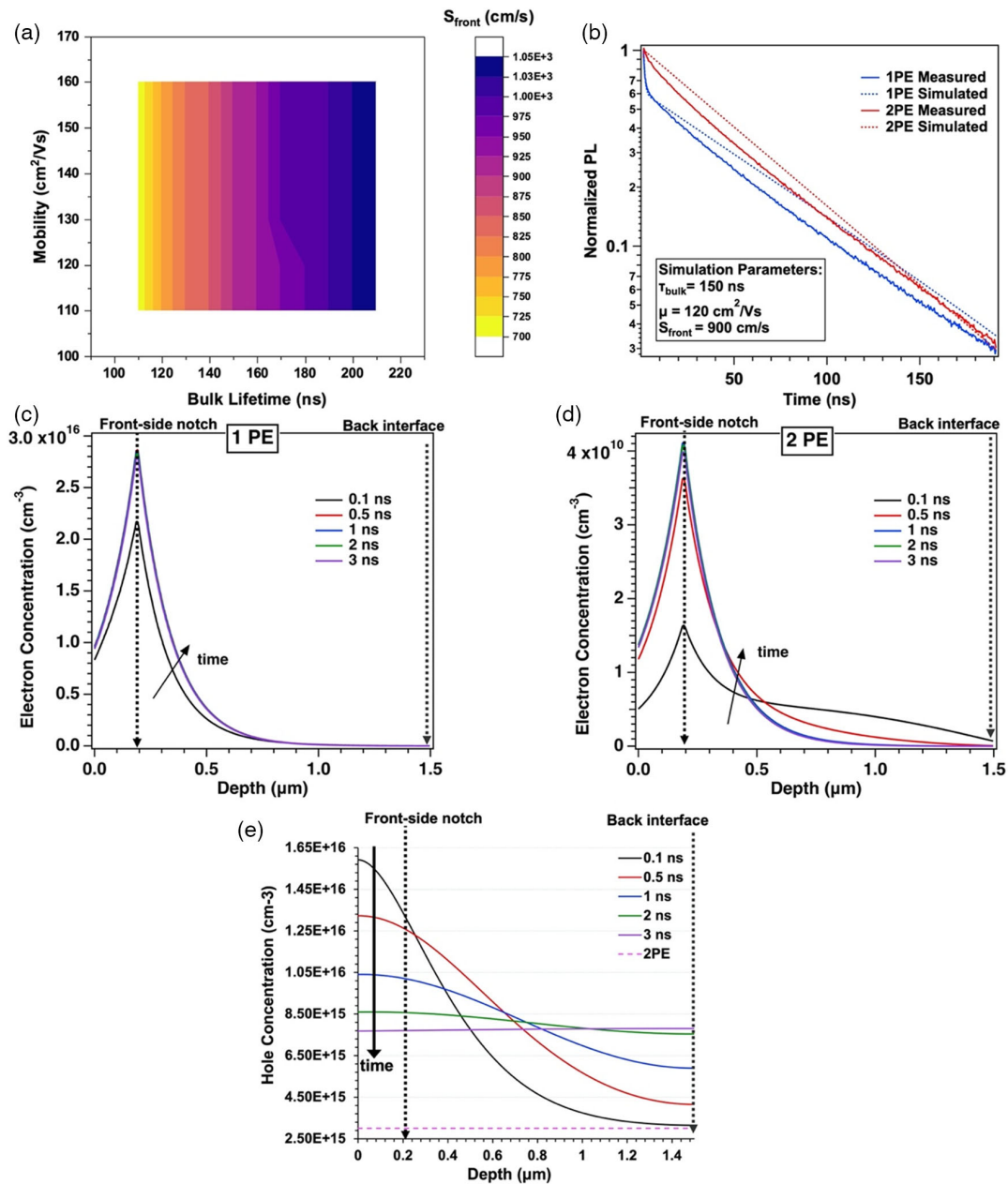


Figure 6. a) Bulk lifetime, mobility, and front interface recombination determined by agreement between measured and simulated 1PE and 2PE TRPL decays. b) Example of simulated (dashed lines) and measured (solid lines) 1PE and 2PE TRPL. c) Simulated electron concentration for 1PE TRPL at time delays after the laser excitation indicated in the legend. Data show electron accumulation at the front-side bandgap notch ($\approx 0.2 \mu\text{m}$) within 0.5 ns. d) Simulated electron concentration for 2PE TRPL for time delays indicated in the legend. Electron density shows comparable behavior to 1PE within 1 ns. e) Hole concentration equilibrates uniformly throughout the absorber within a few nanoseconds after the pulse. Solid lines indicate time-dependent hole density in 1PE measurement, and dashed lines show lower hole density in 2PE measurement.

($\approx 0.2 \mu\text{m}$) within 0.5 ns (as demonstrated by the overlap in $n(x)$ profiles for $t > 0.5$ ns). For 2PE, electrons accumulate within the absorber bulk as well as at the front-side bandgap notch. Electron concentration in the bulk decreases with time as electrons, generated deep in the bulk by 2PE, drift to the front interface via the bandgap gradient. The bandgap gradient is large enough that within 1 ns $n(x)$ profiles are comparable between 1PE and 2PE.

Figure 6e shows the corresponding simulated hole concentrations, $p(x)$. Solid lines correspond to 1PE and the dashed line corresponds to 2PE. For 1PE, as carriers are generated near the front interface, hole concentration is greatest near that interface at short times. As drift and diffusion occur, $p(x)$ equilibrates throughout the absorber within 3 ns. Since the absorption coefficient for 2PE is so small, excess hole concentration is very small compared to the equilibrium carrier concentration of

$3 \times 10^{15} \text{ cm}^{-3}$. Therefore, simulated $p(x)$ for 2PE is equal to the equilibrium carrier concentration and does not change with time. This is represented by the single dashed line in Figure 6e.

Figure 6c–e demonstrates that in less than 3 ns charge carriers have reached equilibrium: for electrons, this occurs at the front-side notch and for holes a constant distribution is reached throughout the absorber. For minority carriers, this is true for both 1PE and 2PE, which indicates that the bandgap grading establishes a strong electric field such that even with excitation from the back side electrons drift to the front within a few nanoseconds.

The S_{front} range in Figure 6a ($700\text{--}1050 \text{ cm s}^{-1}$) is lower than values reported for CdS/CIGS interfaces ($10^3\text{--}10^5 \text{ cm s}^{-1}$)^[14,47,51] and is comparable to atomic layer deposition (ALD) ZnS/CIGS interfaces (810 cm s^{-1}).^[52] Results suggests excellent front interface properties in this CdS/ACIGS structure. The mobility range of $\mu = 110\text{--}160 \text{ cm}^2 \text{ V}^{-1} \text{ s}^{-1}$ is in good agreement with values provided in literature for polycrystalline CIGS, ranging from 20 to $230 \text{ cm}^2 \text{ V}^{-1} \text{ s}^{-1}$.^[14,47,51,53] As previously stated, the simulated bulk lifetime range (110–210 ns) exceeded the 56 ns measured TRPL tail lifetime, and surpassed earlier-generation 19 ns lifetime MiaSolé ACIGS samples.^[20]

3. Conclusion

The path to efficiency improvements in state-of-the-art industrial ACIGS solar cells presented in this work was pursued via targeted mitigation of voltage losses. The solar cells have a radiative voltage $V_{\text{OC,rad}} = 952 \text{ mV}$, within 36 mV of the Shockley–Queisser voltage, $V_{\text{OC,SQ}}$, for 1.24 eV bandgap. It is remarkable that for a pentenary ACIGS absorber manufactured using large-area and rapid industrial fabrication, losses due to semiconductor electronic disorder (bandgap and electrostatic potential fluctuations) are as controlled as for the best small-area solar cells.^[54]

SRH recombination leads to 175 mV voltage loss, which constitutes the difference between $V_{\text{OC,rad}} = 952 \text{ mV}$ and device $V_{\text{OC}} = 777 \text{ mV}$. From defect and device characterization, we demonstrate two strategies that lead to reduced SRH recombination.

First, semiconductor bulk defect density reduction leads to increased minority carrier lifetime and solar cell voltage. As determined by DLTS, the $E_V + 0.58 \text{ eV}$ SRH recombination center defect density is reduced from $1 \times 10^{14} \text{ cm}^{-3}$ ^[20] to $4.3 \times 10^{13} \text{ cm}^{-3}$. This improvement is estimated to increase minority carrier lifetime by a factor of ~ 2.3 , from 19 ns^[20] to about 44 ns. A longer, 56 ns minority carrier lifetime was measured such that a 28 mV voltage increase is attributable to lifetime improvement.

Second, advanced solar cell device architecture mitigates interface recombination losses, with near-record interface passivation implemented via the field effect mechanism. Absorber grading within 200 nm from the front interface (the V-shaped bandgap grading in Figure 2b), achieved by variation in chemical composition, leads to near-interface space charge field. This field repels minority carriers from the interface such that the impact of interface recombination is reduced. Simulations of 1PE and 2PE TRPL data show that effective front interface recombination

velocity is reduced to the $700\text{--}1050 \text{ cm s}^{-1}$ range, which is comparable or lower than the best CIGS interface passivation with state-of-the-art ALD methods.^[52]

Front interface recombination, however, remains a dominant recombination loss. This is evident by a comparison between bulk minority carrier lifetime determined in simulations (110–210 ns) and measured lifetime (56 ns). Due to front interface recombination, effective minority carrier lifetime is shortened from the bulk lifetime by a factor of 2.0–3.8. Further reduction of the front interface recombination could yield additional voltage improvement by a similar amount as bulk defect reduction.

Remaining bulk defects are attributed to the selenium–copper divacancy complex, $V_{\text{Se}}\text{--}V_{\text{Cu}}$, detected by low-temperature PL emission, room-temperature PL excitation, and DLOS measurements. The trap density of $7.2 \times 10^{14} \text{ cm}^{-3}$, calculated from the SSPC, was lower than earlier-reported ACIGS devices,^[20] which suggests K and Cu optimization of Ag-alloyed CIGS absorbers as a route to decreased near-conduction band defect density and concomitant increased J_{SC} stability, doping, and thus V_{OC} .^[40] Mid-gap defects at $E_V + 0.58 \text{ eV}$, measured by DLTS, remain an effective SRH recombination center despite trap density reduction with K and Cu optimization.

In summary, we demonstrate how a combination of semiconductor defect density reduction and device engineering results in improved photovoltaic PCE. These characteristics are achieved in flexible large area (136.5 cm^2) ACIGS solar cells with a bandgap of 1.24 eV and 18.8% efficiency. The same approach can be applied to other PV materials, especially where advanced device architectures are less commonly used.

4. Experimental Section

Absorber and Device Fabrication: ACIGS samples were fabricated by physical vapor deposition (PVD) on stainless steel foil substrates in a MiaSolé production roll-coater tool.^[19,55,56] Prior to the $1.5 \mu\text{m}$ ACIGS absorber deposition, the Mo back electrode was selenized in the PVD chamber. To facilitate K delivery to the ACIGS absorber, the K-doped Mo sputter conditions were optimized compared to previous runs. The nominal Ag concentration in the powder of the sputter targets was $\text{Ag}/(\text{Ag}+\text{Cu}) = 0.1\%$ or 10%. This transferred reasonably well to the deposited absorber as shown in Figure 2c. The ACIGS surface was also grown Cu-poor to allow K diffusion to the top of the absorber. A 30 nm CdS buffer layer was deposited on the ACIGS absorber, followed by a 100 nm intrinsic ZnO layer and 300–400 nm conductive ZnO layer such that the latter two layers form the transparent conducting oxide (TCO) layer. The CdS and ZnO layers were deposited via sputtering on the roll-coater tool. The 136.5 cm^2 area devices were cut from the full material stack from the roll-coater and a metal grid electrode was used to connect to the top of the TCO.

Device Characterization: ACIGS device performance parameters were determined by illuminated $J\text{--}V$ measurements. Measurements were carried out at room temperature under 1-sun AM 1.5 G illumination, with four-point probe measurements such that V_{OC} , J_{SC} , FF , and efficiency (η) were extracted. EQE spectra were measured from 350 to 1200 nm at room temperature with no bias illumination (i.e., dark EQE) or voltage bias. C–V profiles were measured using a Boonton 7200 capacitance meter at a measurement frequency of 1 MHz at room temperature with biases from -1 to 0 V, from which doping profiles were calculated using standard Mott–Schottky analysis.^[57] Samples were kept in the dark for at least 10 h before measurement to ensure traps were in their equilibrium state. The Q factor for these samples was always greater than 5 and though the ideal

was >10, comparisons of series and parallel models showed accurate capacitance measurement.^[57]

Composition Characterization: The ACIGS film stack composition was determined via AES sputter depth profiling on a Physical Electronics Model 710 AES nanoprobe. A 5 kV, 20 nA primary beam was used for analysis. Sputtering was performed with a 2 kV monoatomic argon beam ($8 \mu\text{A mm}^{-2}$). AES sensitivity factors for selenium, indium, and gallium were determined using a procedure described previously.^[58]

An time of flight (IonTOF) 5 SIMS was used to measure the elemental composition throughout the structure. The primary depth profiling beam was 1.0 keV Cs⁺ with a current of 111 nA, and a 30 keV Bi⁺ beam with a current of 184 pA was used for analysis. Positive secondary ions were detected; molecular species which combined the atom of interest with Cs were used where necessary to achieve improved sensitivity. Without a reference standard by which to determine ion yield from SIMS, the elemental composition was calculated in two steps. First, all SIMS count rates were normalized to the total counts to correct for changes in sputtering rate and changes in ion yields. Second, for each element, the values were renormalized by an overall factor determined from AES compositions.

Deep-Level Transient and Deep-Level Optical Spectroscopy: To characterize the impact of deep-level defects on device performance, DLTS and DLOS were performed on the ACIGS solar cells, which allowed for characterization of traps throughout the CIGS bandgap. DLTS, which allows one to observe traps up to approximately mid-gap, was performed with a custom setup using a Lakeshore TTP4 probe station and a Boonton 7200 capacitance meter.^[59] Traps were filled using a 0 V fill pulse, and trap emission was measured at -1 V. The transients were analyzed using the double boxcar analysis, with rate windows from 0.8 to 2000 s^{-1} .^[60] DLOS was used to characterize deep traps in the upper half of the *p*-type bandgap by shining monochromated light of a known flux onto the sample and measuring the resulting capacitance transient and SSPC.^[41] The trap concentrations were calculated for both DLTS and SSPC using $2N_A\Delta C/C_\infty$ where N_A is the acceptor doping concentration, ΔC is the change in capacitance due to the trap emission, and C_∞ is the steady-state capacitance in the dark at the reverse bias (i.e., -1 V). For DLTS, these calculations were corrected for the lambda effect, which accounted for smaller volume where the traps modulated during the measurement compared with the entire depletion volume that was assumed in the simple equation. For DLTS, ΔC was calculated from the peak height of the double boxcar analysis.^[59] For SSPC, an onset in the spectrum indicated a trap and the trap concentration was extracted from the step height. Onset trap energies from the SSPC had more error because of the slow onsets, so trap energies were more accurately determined by fitting the DLOS spectrum with optical cross-section models. This also allowed fitting to determine whether the emission involved lattice relaxation (i.e., Franck–Condon energy) as well. For ACIGS, the Franck–Condon energy was minimal, so the Lučovský model was sufficient to extract the trap energy.^[39]

PL Characterization: PL and TRPL analyses were applied to the ACIGS/CdS films. PL emission spectroscopy used excitation at 632.8 nm (HeNe continuous wave laser) and a SpectraPro HRS 300 spectrograph. Excitation was varied in the 8×10^{-4} –0.21 Suns range (fluence 2.7×10^{14} – 6.7×10^{16} photons $\text{cm}^{-2} \text{ s}^{-1}$, power 1–250 μW). Sample temperature was controlled with a closed loop He cryostat.

TRPL was measured with pulsed laser excitation (0.3 ps pulses at a 1.1 MHz laser repetition rate) using time-correlated single-photon counting.^[61] Because one-photon and two-photon absorption coefficients differ, carrier dynamics after photogeneration near the front interface of the solar cell (generation with 1PE, 640 nm) and in the absorber layer (generation with 2PE, 1200 nm) could be investigated. The excitation wavelength was controlled by tuning the optical parametric amplifier (OPA). For 1PE studies, 640 nm, 18 μW to 1.0 mW (1.9×10^{12} – 1×10^{17} photons $\text{cm}^{-2} \text{ pulse}^{-1}$) excitation was used. The resulting carrier generation close to the front interface led to electron movement (induced by the band-edge shift), diffusion, and interface recombination. From the lowest to the middle excitation fluence range, photogenerated carriers were not expected to screen electric fields in the material, thus providing optical probes for the space charge field near the front interface. For 2PE, laser pulses at

1200 nm, 4.5 mW average power (160 W cm^{-2}) were employed to probe recombination in the bulk of the absorber.^[46] TRPL simulation code developed by Weiss et al.^[33] was used to simulate 1PE and 2PE TRPL decays and to estimate bulk recombination lifetime (τ_{bulk}), front surface recombination velocity (S_{front}), mobility (μ), and back surface recombination velocity (S_{back}).

PL excitation spectra were measured with the OPA-based TRPL setup where wavelength variation was employed to directly excite defect states in the absorber bandgap. PL excitation data were generated by integrating TRPL decays at each excitation energy, from 1170 to 1460 nm, with detection at 1000 nm. Such measurements provide sensitive optical probes for near-bandgap defect states, which can have low radiative efficiency but can be characterized from their absorption signatures in the PL excitation spectra.^[36]

Acknowledgements

This work was authored in part by the National Renewable Energy Laboratory, operated by Alliance for Sustainable Energy, LLC, for the USA Department of Energy (DOE) under contract no. DE-AC36-08GO28308. Funding provided by USA Department of Energy Office of Energy Efficiency and Renewable Energy Solar Energy Technologies Office. The views expressed in the article do not necessarily represent the views of the DOE or the USA Government. The USA Government retains and the publisher, by accepting the article for publication, acknowledges that the USA Government retains a nonexclusive, paid-up, irrevocable, worldwide license to publish or reproduce the published form of this work, or allow others to do so, for USA Government purposes. This material is based upon work supported by the USA Department of Energy's Office of Energy Efficiency and Renewable Energy (EERE) under the Solar Energy Technology Office (SETO) Award Number DE-EE0008755. This material makes use of the TOF-SIMS system at the Colorado School of Mines, which was supported by the National Science Foundation under grant no. 1 726 898. This report was prepared as an account of work sponsored by an agency of the USA Government. Neither the USA Government nor any agency thereof, nor any of their employees, makes any warranty, express or implied, or assumes any legal liability or responsibility for the accuracy, completeness, or usefulness of any information, apparatus, product, or process disclosed, or represents that its use would not infringe privately owned rights. Reference herein to any specific commercial product, process, or service by trade name, trademark, manufacturer, or otherwise does not necessarily constitute or imply its endorsement, recommendation, or favoring by the USA Government or any agency thereof. The views and opinions of authors expressed herein do not necessarily state or reflect those of the USA Government or any agency thereof.

Conflict of Interest

The authors declare no conflict of interest.

Data Availability Statement

The data that support the findings of this study are available from the corresponding author upon reasonable request.

Keywords

absorber grading, ACIGS, defects, solar cells, voltage losses

Received: March 14, 2022

Revised: April 25, 2022

Published online: May 6, 2022

- [1] *Solar Frontier Achieves World Record Thin-Film Solar Cell Efficiency of 23.35%*, https://www.solar-frontier.com/eng/news/2019/0117_press.html, accessed: March, 2022.
- [2] M. Green, E. Dunlop, J. Hohl-Ebinger, M. Yoshita, N. Kopidakis, X. Hao, *Prog. Photovoltaics: Res. Appl.* **2021**, 29, 3.
- [3] P. Jackson, D. Hariskos, R. Wuerz, W. Wischmann, M. Powalla, *Phys. Status Solidi RRL: Rapid Res. Lett.* **2014**, 8, 219.
- [4] M. Krause, A. Nikolaeva, M. Maiberg, P. Jackson, D. Hariskos, W. Witte, J. A. Márquez, S. Levchenko, T. Unold, R. Scheer, *Nat. Commun.* **2020**, 11, 1.
- [5] S. Rühle, *Solar Energy* **2016**, 130, 139.
- [6] T. Kato, *Jpn. J. Appl. Phys.* **2017**, 56, 4S.
- [7] T. Feurer, P. Reinhard, E. Avancini, B. Bissig, J. Löckinger, P. Fuchs, R. Carron, T. P. Weiss, J. Perrenoud, S. Stutterheim, *Prog. in Photovoltaics: Res. Appl.* **2017**, 25, 7.
- [8] F. Larsson, N. S. Nilsson, J. Keller, C. Frisk, V. Kosyak, M. Edoff, T. Törndahl, *Prog. Photovoltaics: Res. Appl.* **2017**, 25, 755.
- [9] M. A. Contreras, L. M. Mansfield, B. Egaas, J. Li, M. Romero, R. Noufi, E. Rudiger-Voigt, W. Mannstadt, *Prog. Photovoltaics: Res. Appl.* **2012**, 20, 843.
- [10] P. T. Erslev, J. Lee, G. M. Hanket, W. N. Shafarman, J. D. Cohen, *Thin Solid Films* **2011**, 519, 7296.
- [11] R. Mickelsen, W. S. Chen, in *Proc. Inter. Conf. on Ternary and Multinary Compounds*, Pittsburgh, PA, **1987**.
- [12] H. W. Schock, in *12th European Photovolt. Solar Energy Conf.* Amsterdam, The Netherlands April **1994**.
- [13] W. N. Shafarman, R. Klenk, B. E. McCandless, *J. Appl. Phys.* **1996**, 79, 7324.
- [14] J. V. Li, S. Grover, M. A. Contreras, K. Ramanathan, D. Kuciauskas, R. Noufi, *Sol. Energy Mater. Sol. Cells* **2014**, 124, 143.
- [15] J. Tuttle, M. Contreras, K. Ramanathan, S. Asher, R. Bhattacharya, T. Berens, J. Keane, R. Noufi, in *AIP Conference Proceedings*, Vol. 394, American Institute of Physics **1997** <https://doi.org/10.1063/1.52889>.
- [16] J. Boyle, B. McCandless, G. Hanket, W. Shafarman, *Thin Solid Films* **2011**, 519, 7292.
- [17] M. Edoff, T. Jamar, N. S. Nilsson, E. Wallin, D. Högström, O. Stolt, O. Lundberg, W. Shafarman, L. Stolt, *IEEE J. Photovoltaics* **2017**, 7, 1789.
- [18] M. Richards, *MiaSolé Achieves Flexible Substrate Thin-Film Solar Cell Efficiency of 20.56 Percent*, <https://miasole.com/miasole-achieves-flexible-substrate-thin-film-solar-cell-efficiency-of-20-56-percent/>, accessed: March, 2022.
- [19] M. Richards, *MiaSolé Breaks World Record Again: Large Area Flexible Photovoltaic Module with 18.64% Efficiency*, <https://miasole.com/miasole-breaks-world-record-again-large-area-flexible-photovoltaic-module-with-18-64-efficiency/>, accessed: March, 2022.
- [20] A. J. Ferguson, R. Farshchi, P. K. Paul, P. Dippo, J. Bailey, D. Poplavskyy, A. Khanam, F. Tuomisto, A. R. Arehart, D. Kuciauskas, *J. Appl. Phys.* **2020**, 127, 215702.
- [21] U. Rau, B. Blank, T. C. Müller, T. Kirchartz, *Phys. Rev. Appl.* **2017**, 7, 044016.
- [22] R. Carron, C. Andres, E. Avancini, T. Feurer, S. Nishiwaki, S. Pisoni, F. Fu, M. Lingg, Y. E. Romanyuk, S. Buecheler, *Thin Solid Films* **2019**, 669, 482.
- [23] L. Krückemeier, U. Rau, M. Stollerfoht, T. Kirchartz, *Adv. Energy Mater.* **2020**, 10, 1902573.
- [24] B. Huang, S. Chen, H.-X. Deng, L.-W. Wang, M. A. Contreras, R. Noufi, S.-H. Wei, *IEEE J. Photovoltaics* **2013**, 4, 477.
- [25] J. Pohl, K. Albe, *Phys. Rev. B* **2013**, 87, 245203.
- [26] J. Chantana, Y. Kawano, T. Nishimura, A. Mavlonov, T. Minemoto, *Sol. Energy Mater. Sol. Cells* **2020**, 210, 110502.
- [27] S. Paul, S. Grover, I. L. Repins, B. M. Keyes, M. A. Contreras, K. Ramanathan, R. Noufi, Z. Zhao, F. Liao, J. V. Li, *IEEE J. Photovoltaics* **2018**, 8, 871.
- [28] G. Regmi, A. Ashok, P. Chawla, P. Semalti, S. Velumani, S. N. Sharma, H. Castaneda, *J. Mater. Sci.: Mater. Electron.* **2020**, 31, 7286.
- [29] A. Mudryi, V. Gremenok, A. Karotki, V. Zaleski, M. Yakushev, F. Luckert, R. Martin, *J. Appl. Spectrosc.* **2010**, 77, 371.
- [30] M. Powalla, P. Jackson, W. Witte, D. Hariskos, S. Paetel, C. Tschamber, W. Wischmann, *Sol. Energy Mater. Sol. Cells* **2013**, 119, 51.
- [31] I. Repins, S. Glynn, J. L. Duenow, T. J. Coutts, W. K. Metzger, M. A. Contreras, *Thin Film Solar Technol.* **2009**, 7409, 156.
- [32] M. R. Golobostanfard, H. Abdizadeh, *RSC Adv.* **2016**, 6, 11903.
- [33] T. P. Weiss, B. Bissig, T. Feurer, R. Carron, S. Buecheler, A. N. Tiwari, *Sci. Rep.* **2019**, 9, 1.
- [34] M. Igalson, M. Cwil, M. Edoff, *Thin Solid Films* **2007**, 515, 6142.
- [35] S. Lany, A. Zunger, *J. Appl. Phys.* **2006**, 100, 113725.
- [36] S. Jensen, A. Kanevce, L. Mansfield, S. Glynn, S. Lany, D. Kuciauskas, *Sci. Rep.* **2017**, 7, 1.
- [37] T. Schmidt, K. Lischka, W. Zulehner, *Phys. Rev. B* **1992**, 45, 8989.
- [38] M. J. Romero, H. Du, G. Teeter, Y. Yan, M. M. Al-Jassim, *Phys. Rev. B* **2011**, 84, 165324.
- [39] G. Lucovsky, *Solid State Commun.* **1965**, 3, 299.
- [40] P. Paul, T. Jamar, L. Stolt, A. Rockett, A. Arehart, in *2017 IEEE 44th Photovoltaic Specialist Conf. Proc.* **2017**, p. 30.
- [41] P. Blood, J. Orton, *Rep. Prog. Phys.* **1978**, 41, 157.
- [42] S.-H. Wei, S. Zhang, A. Zunger, *Appl. Phys. Lett.* **1998**, 72, 3199.
- [43] J. I. Deitz, P. K. Paul, R. Farshchi, D. Poplavskyy, J. Bailey, A. R. Arehart, D. W. McComb, T. J. Grassman, *Adv. Energy Mater.* **2019**, 9, 1901612.
- [44] S. Karki, P. K. Paul, G. Rajan, T. Ashrafee, K. Aryal, P. Pradhan, R. W. Collins, A. Rockett, T. J. Grassman, S. A. Ringel, *IEEE J. Photovoltaics* **2016**, 7, 665.
- [45] P. Paul, D. Cardwell, C. Jackson, K. Galiano, K. Aryal, J. Pelz, S. Marsillac, S. Ringel, T. Grassman, A. Arehart, *IEEE J. Photovoltaics* **2015**, 5, 1482.
- [46] D. Kuciauskas, A. Kanevce, J. M. Burst, J. N. Duenow, R. Dhere, D. S. Albin, D. H. Levi, R. K. Ahrenkiel, *IEEE J. Photovoltaics* **2013**, 3, 1319.
- [47] D. Kuciauskas, J. V. Li, M. A. Contreras, J. Pankow, P. Dippo, M. Young, L. M. Mansfield, R. Noufi, D. Levi, *J. Appl. Phys.* **2013**, 114, 154505.
- [48] W. K. Metzger, I. L. Repins, M. A. Contreras, *Appl. Phys. Lett.* **2008**, 93, 022110.
- [49] S. Minoura, K. Kodaera, T. Maekawa, K. Miyazaki, S. Niki, H. Fujiwara, *J. Appl. Phys.* **2013**, 113, 063505.
- [50] A. Kanevce, D. Levi, D. Kuciauskas, *Prog. Photovoltaics: Res. Appl.* **2014**, 22, 1138.
- [51] S. A. Jensen, S. Glynn, A. Kanevce, P. Dippo, J. V. Li, D. H. Levi, D. Kuciauskas, *J. Appl. Phys.* **2016**, 120, 063106.
- [52] A. Hultqvist, J. V. Li, D. Kuciauskas, P. Dippo, M. A. Contreras, D. H. Levi, S. F. Bent, *Appl. Phys. Lett.* **2015**, 107, 033906.
- [53] D. Kuciauskas, J. V. Li, A. Kanevce, H. Guthrey, M. Contreras, J. Pankow, P. Dippo, K. Ramanathan, *J. Appl. Phys.* **2015**, 117, 185102.
- [54] M. H. Wolter, R. Carron, E. Avancini, B. Bissig, T. P. Weiss, S. Nishiwaki, T. Feurer, S. Buecheler, P. Jackson, W. Witte, *Prog. Photovoltaics: Res. Appl.* **2021**, 1.
- [55] J. Bailey, G. Zapalac, D. Poplavskyy, in *2016 IEEE 43rd Photovoltaic Specialist Conf. Proc.* **2016**, p. 2135.
- [56] R. Farshchi, B. Hickey, G. Zapalac, J. Bailey, D. Spaulding, D. Poplavskyy, in *2016 IEEE 43rd Photovoltaic Specialist Conf. Proc.* **2016**, p. 2157.
- [57] D. Schroeder, *John Wiley*, John Wiley & Sons Inc., Hoboken, NJ **1998**.

[58] C. L. Perkins, B. Egaas, I. Repins, B. To, *Appl. Surf. Sci.* **2010**, 257, 878.

[59] A. Arehart, A. Allerman, S. Ringel, *J. Appl. Phys.* **2011**, 109, 114506.

[60] D. Lang, *J. Appl. Phys.* **1974**, 45, 3023.

[61] D. Kuciauskas, J. N. Duenow, A. Kanevce, J. V. Li, M. R. Young,

P. Dippo, D. H. Levi, in *in 2012 38th IEEE Photovoltaic Specialists*

Conf. Proc. **2012**, p. 001721.